

Unveiling local magnetic moments in copper-oxide atomic junctions

Marcel Strohmeier, Wolfgang Belzig, and Elke Scheer
Department of Physics, University of Konstanz, 78457 Konstanz, Germany

Samanwita Biswas and Regina Hoffmann-Vogel
Institute of Physics and Astronomy, University of Potsdam, 14476 Potsdam-Golm, Germany
(Dated: March 12, 2026)

Incorporating oxygen into metallic atomic-scale junctions modifies the interatomic bonding and may even promote the formation of monoatomic chains. In the specific case of copper oxide, first-principles studies have predicted the emergence of ferromagnetic ground states, attributing certain atomic configurations with spin filtering capabilities. By means of low-temperature transport measurements, we provide a series of experimental evidence indicating the presence of local magnetism in air oxidized mechanically controllable copper break junctions. Our investigations on ultimately small contacts range from magnetotransport measurements to the analysis of anomalous shot noise in the presence of strong zero-bias anomalies. The analysis of the latter allows to determine the spin polarization (SP) of the current and that is interpreted with the Kondo physics picture.

I. INTRODUCTION

Copper is a key material for electrical interconnects in the semiconductor industry, making a detailed understanding of its conductance properties essential. Despite its electronic similarity to Ni, with only one extra electron, opening the $4s$ shell in case of Cu, with nearly free-electron-like transport, Cu remains slightly diamagnetic, whereas Ni exhibits robust itinerant ferromagnetism. This contrast highlights the delicate balance between electronic structure and magnetism in transition metals. Notably, Cu can acquire magnetic character through oxidation, forming Cu(I) oxide and Cu(II) oxide. CuO_x themselves display a rich variety of magnetic phases, ranging from bulk diamagnetism to complex multiferroic behavior [1–4]. At reduced dimensions, ferromagnetic signatures have been observed in several nanoscale systems [5–15]. In many cases, non-stoichiometric surface magnetism has been proposed as a plausible explanation [8–10, 12–15]. Research on atomic-scale entities such as clusters or monoatomic chains, however, remains a largely unexplored field, where fundamental questions about the emergence of magnetism and its coupling to electronic transport persist.

Atomic-scale junctions formed from nominally nonmagnetic metals provide a particularly appealing platform to explore how oxidation and atomic-scale confinement can profoundly modify magnetic and transport properties. Cu_xO atomic junctions are especially intriguing in this regard. Oxygen incorporation introduces partially filled p orbitals and enhances hybridization with Cu d states, creating favorable conditions for the formation of localized magnetic moments [16]. First-principles calculations predict that Cu-O monoatomic chains can stabilize ferromagnetic ground states, exhibit strong SP, and act as efficient spin filters [17], despite the absence of magnetism in pristine Cu chains [16]. Experimentally, oxygen assisted formation of elongated atomic chains in mechanically controllable break junctions has been observed, accompanied by a pronounced suppression of con-

ductance relative to clean Cu contacts [18]. However, direct experimental evidence linking these structural motifs to magnetic order or correlated electron phenomena remains scarce, and the microscopic mechanisms governing spin dependent transport in Cu_xO atomic junctions are still poorly understood [17–19].

II. EXPERIMENTAL TECHNIQUES

The experiments were carried out using mechanically controlled thin-film break junctions (thin-film MCBJs). We fabricate the samples by electron beam lithography and electron beam evaporation in lift-off technique in combination with a subsequent oxygen plasma treatment to define narrow suspended Cu bridges on an insulating substrate. The purity of the starting material is Cu $>99.999\%$ with a Fe content of 0.01 ppm. The thickness and width of the pristine nanowire are about 100 nm, guaranteeing a metallic core despite the plasma treatment [20, 21].

All measurements were carried out in cryogenic vacuum at a base temperature of 4.2 K. To reach these environmental condition, two complementary measurement inserts were used in a helium bath (wet) cryostat: one dedicated to magnetotransport measurements and the other one specifically designed for shot noise experiments [21, 22].

III. RESULTS

First we confirm the known behavior of clean metallic Cu atomic contacts [18, 23–25]. To investigate whether oxygen incorporation induces magnetic signatures in the electronic transport properties of atomic-scale Cu junctions, we then study MCBJs that were intentionally oxidized prior to low-temperature measurements. Oxidation was achieved via passive exposure to ambient air, combined with a controlled pre-cooling procedure designed to

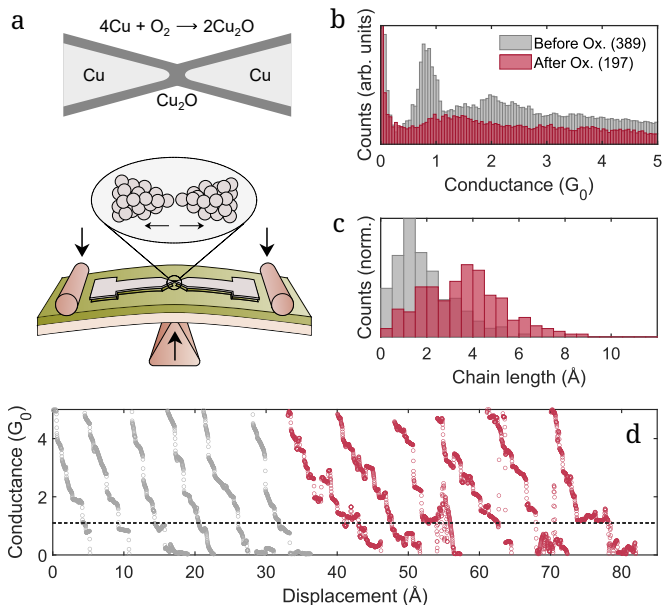


FIG. 1. Analysis of the opening traces recorded on an air oxidized Cu MCBJ, comparing measurements taken during two consecutive cool-downs. (a) Cartoon of the oxidized atomic contact. The light gray areas indicate the metallic Cu, the dark gray the oxidized areas at the surface of the leads and in the contact region. (b) Conductance histogram constructed from all opening curves. (c) Distribution of chain lengths extracted from the traces. (d) Examples of individual opening traces. Gray/red: First cool-down (without/with breaking the junction at room temperature)

enhance oxygen incorporation into the nano-constriction. Specifically, pristine Cu junctions were first ruptured in air into the tunneling regime and subsequently re-closed before cooling down. This protocol promotes surface oxidation at the rupture site and increases the likelihood that subsequent low-temperature breaks occur within the oxidized region.

Already after a single rupture in air, pronounced changes in the contact formation are observed. Upon re-closing, the resistance often does not fully recover its initial metallic value and larger mechanical displacements are required to re-establish contact. These observations indicate a modified atomic structure at the junction, consistent with partial oxidation of the Cu constriction. In practice, this breaking and closing protocol can be repeated only a limited number of times (mostly two or three cycles), as excessive opening may prevent reliable contact reformation.

A. Conductance histogram and chain lengths

A first indication of oxygen incorporation is provided by conductance traces and histograms compiled from these. In the histograms, compared to pristine Cu junctions, air oxidized contacts exhibit a strong suppression of the

characteristic conductance peaks near integer multiples of G_0 , accompanied by an enhanced weight at low conductance values. This behavior reflects the stabilization of highly resistive atomic configurations and is consistent with earlier reports on oxygen assisted chain formation in Cu break junctions [18].

Further insight is obtained from the analysis of individual opening traces and their associated chain lengths. After calibrating the electrode displacement, the final stage of each rupture trace was analyzed by defining the chain length as the displacement between conductance values of $1.1 G_0$ and $0.05 G_0$. In oxidized junctions, the conductance evolution within this window is highly non-monotonic and varies strongly from trace to trace, indicative of a complex atomic rearrangement process involving Cu-O units.

B. Magnetoconductance

Magnetotransport measurements were performed on mechanically fixed atomic Cu/Cu_xO junction configurations at $T \approx 4.2$ K by sweeping a magnetic field perpendicular to the sample plane. The conductance $G = I/V$ was recorded continuously while ramping the field between $\pm B_{\max}$, and only complete sweeps between positive and negative maximum fields were evaluated. Throughout all measurements, a constant bias voltage of 10 mV was applied.

Fig. 2 summarizes the key experimental observations for air oxidized junctions. Panel (a) shows a collection of magnetoconductance (MC) traces exhibiting pronounced non-monotonic behavior as a function of magnetic field. Both positive and negative MC responses are observed, with relative conductance changes reaching several tens of percent. The curves are mainly symmetric upon field reversal but often hysteretic, and their shapes vary strongly from contact to contact. Both positive and negative MC responses are observed, with relative conductance changes reaching several tens of percent. To facilitate comparison, the traces are vertically shifted and re-scaled.

For each MC trace, the corresponding current-voltage characteristics measured immediately prior to the field sweep are shown in panel (b). All $dI/dV - V$ curves are smooth within the explored bias range, showing small variations on the scale of a few mV as typical for conductance fluctuations [24], without pronounced zero-bias anomalies (ZBAs) or other spectroscopic signatures.

The magnitude of the field induced conductance variation is quantified by the maximum magnetoconductance ratio

$$\text{MCR}_{\max} = \max \left(\frac{|G(B) - G(0)|}{G(0)} \right), \quad (1)$$

extracted from each sweep. Figure 2 (c) displays MCR_{\max} as a function of the zero-field conductance for all continuous MC sweeps. Significant MC signals are

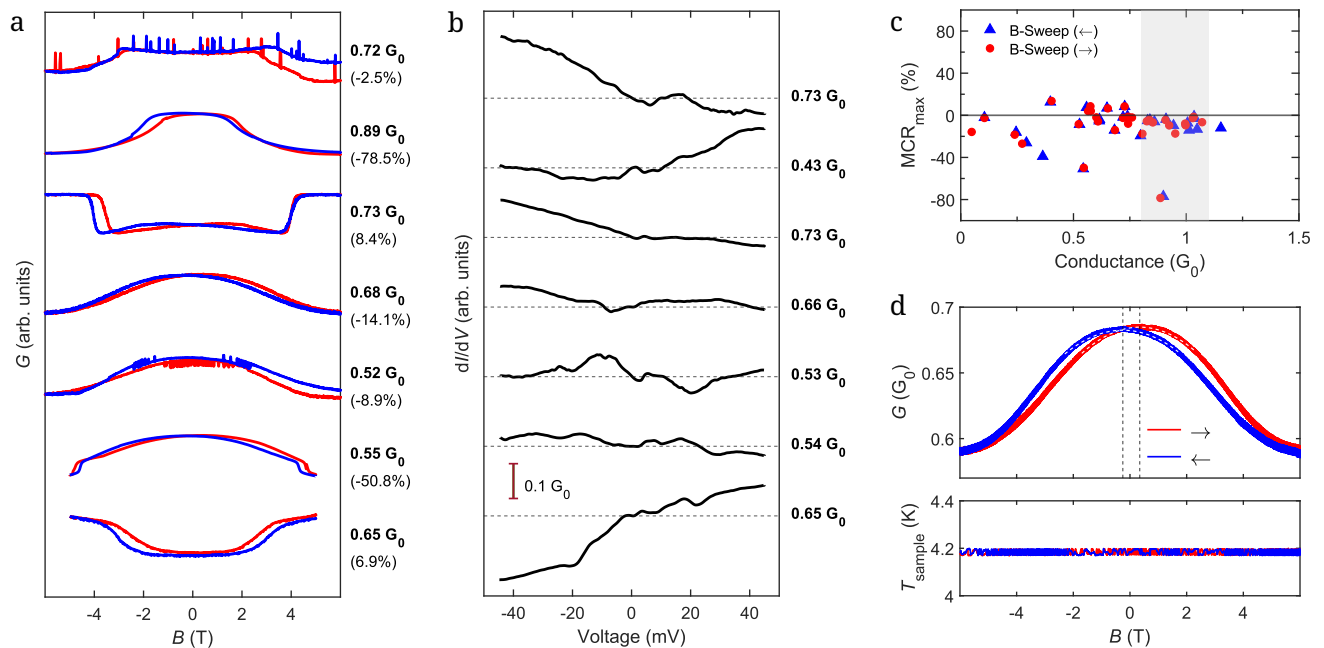


FIG. 2. Magnetoconductance (MC) measurements on atomic Cu/Cu_xO contacts. (a) Representative non-monotonic MC traces recorded after ambient-air exposure in a semi-broken state. Curves are scaled and vertically off-set for clarity. (b) Corresponding I - V characteristics measured prior to each MC sweep, shown with vertical offsets only (see conductance scale bar). In all measurements, the magnetic field is applied perpendicular to the sample plane and swept between ± 5 T or ± 6 T. Blue (red) traces denote the return (forward) sweep. Labels indicate the zero-bias conductance (bold) and the maximum magnetoconductance ratio MCR_{\max} (in brackets). (c) MCR_{\max} as a function of zero-field conductance for all continuous MC sweeps of the same sample; different symbols distinguish sweep directions. (d) Example MC trace measured during a second cool-down after air exposure, showing nonlinear and hysteretic behavior at $G < 1G_0$ (upper panel). The simultaneously recorded sample temperature remains constant throughout the field sweep (lower panel).

predominantly found for junctions with conductances below $1G_0$, i.e. in a range corresponding to oxidized atomic configurations or short Cu-O chains. Both sweep directions yield comparable results, indicating that the extracted MCR values are robust. The MCR values and the field scale of the variation corresponds to the observations made for atomic contacts from the strong paramagnets Pt, Pd and Ir [21, 26, 27] and indicate the emergence of local magnetic moments.

To exclude thermal artifacts due to eddy-current heating, Fig. 2 (d) shows a representative MC trace together with the simultaneously recorded sample temperature. The temperature remains constant during the entire magnetic-field sweep, demonstrating that the observed conductance variations cannot be attributed to field induced heating or temperature drifts. Combined with the absence of abrupt conductance jumps, magnetostriction or thermal effects are ruled out as the dominant origin of the MC features.

C. Zero-bias anomalies and Fano line-shapes

Signatures of magnetic order may also occur as spectroscopic features in current-voltage characteristics. The most prominent one stems from the Kondo effect, a

many-body phenomenon which was first discovered in metals containing dilute magnetic impurities and manifests itself in nanocontacts as a ZBA in the differential conductance. At the atomic scale, such resonances commonly acquire a Fano line shape due to quantum interference between a localized magnetic moment and a continuum of conduction channels [28].

In oxidized Cu break junctions, weak ZBAs with conductance values well below $1G_0$ are observed in a subset of atomic contacts. Representative examples of dI/dV spectra are shown in Fig. 3 (a,b), together with fits to the standard Fano expression [29]

$$\frac{dI}{dV}(V) = g_0 + A \frac{(q + \varepsilon)^2}{1 + \varepsilon^2}, \quad \varepsilon = \frac{eV - \varepsilon_K}{\Gamma_K}. \quad (2)$$

From these fits, the resonance amplitude A , shape factor q , and the Kondo temperature T_K are extracted. With $\Gamma_K = k_B T_K$ the Kondo parameters can be further linked to the impurity level occupation [29]

$$n_d = 1 - \frac{2}{\pi} \arctan \left(\frac{\varepsilon_K}{k_B T_K} \right). \quad (3)$$

A statistical analysis of all spectra with $A > 0.01G_0$ reveals a broad distribution of Kondo temperatures (Fig. 3

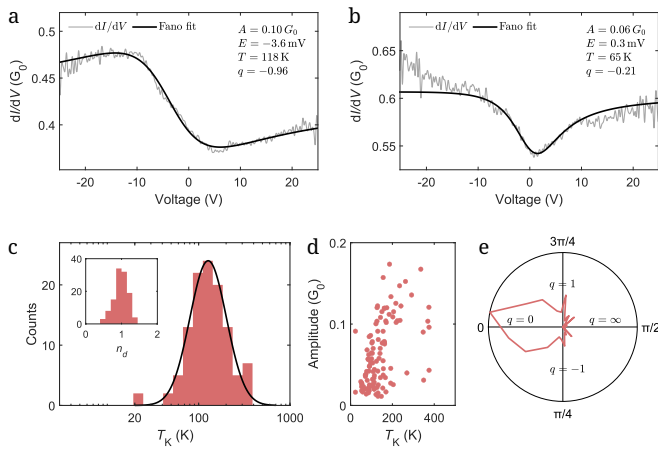


FIG. 3. Analysis of the Kondo effect in an oxidized Cu MCBJ: (a), (b) Examples of dI/dV curves exhibiting Fano line shapes. A fit to Eq. (2) is shown by the solid line. (c) Histogram of the Kondo temperature T_K and occupation number n_d (inset) across all contacts with $A > 0.01 G_0$. A log-normal distribution is fitted to the T_K data. (d) Scatter plot of A versus T_K . (e) Polar plot with $\alpha = \arctan(q)$, representing the distribution of the shape factor $|q| \in [0, \infty)$.

(c)), which is well described by a log-normal form, reflecting the exponential dependence of T_K on the microscopic parameters of the junction. The mean value, $\overline{T_K} \approx 150$ K, lies in the range reported for atomic-scale Kondo systems in transition metal contacts. The inferred impurity occupation is centered close to unity, consistent with a predominantly singly occupied magnetic level.

In Fig. 3 (d) we plot A vs. T_K , revealing no systematic correlation between both parameters. The amplitudes A are similar to those reported for ferromagnetic nanocontacts [29].

The distribution of Fano parameters shows a strong preference for dip-like or weakly asymmetric resonances with $|q| \lesssim 1$ [Fig. 3 (e)]. This indicates that transport through Cu_xO atomic contacts is dominated by a background channel i.e., with s -level character, while the Kondo resonance contributes mainly via destructive interference. Such behavior is consistent with strong hybridization between oxygen related states and the metallic Cu electrodes.

Overall, the observed Fano line shapes provide spectroscopic evidence for localized magnetic moments in oxidized Cu atomic junctions for a small subset of the junctions. While most ZBAs are weak, they establish a direct link between oxygen incorporation and many-body spin correlations, forming the basis for the anomalous shot noise behavior discussed in the following section. We note that in metallic Cu contacts (studied in cool-downs before oxidation) no such ZBAs were observed. However, it has to be taken into account that the probability of contact formation with conductance values below $1G_0$ is very low.

D. Shot noise measurements

In addition to MC measurements, we study the shot noise of atomic contacts at $B = 0$. These non-equilibrium current fluctuations the amplitude of which is proportional to the current for quantum coherent conductors with linear current-voltage characteristics provide direct access to the number of conduction channels, their transmission probabilities, and possible SP [30–32]. The noise measurement setup is shown in Fig. 4 (a) and follows the same design as in our previous study [22]. It is optimized for direct shot noise detection using a current amplifier with an extended bandwidth up to 800 kHz.

1. Fano factor

Being in the quantum-coherent regime, the shot noise is first analyzed within the Landauer formalism. For a system at finite temperature T , the corresponding expression for the noise power reads [33]

$$S_I = eVG_0 \coth\left(\frac{eV}{2k_B T}\right) \sum_{i,\sigma} \tau_{i,\sigma} (1 - \tau_{i,\sigma}) + 2k_B T G_0 \sum_{i,\sigma} \tau_{i,\sigma}^2, \quad (4)$$

where V is the applied bias voltage and k_B denotes the Boltzmann constant. To assess the Fano factor $F = S_I/2e\langle I \rangle = \sum_{i,\sigma} \tau_{i,\sigma} (1 - \tau_{i,\sigma}) / \sum_{i,\sigma} \tau_{i,\sigma}$ and, hence, the degree of SP

$$SP = \frac{|G_\uparrow - G_\downarrow|}{G_\uparrow + G_\downarrow}, \quad (5)$$

we follow the methodology of Kumar *et al.* [34] by introducing the normalized noise $Y = [S_I(V) - S_I(0)]/S_I(0)$ and normalized voltage $X = x \coth(x)$ with $x = eV/2k_B T$. Handling the data via the linear relation

$$Y = F(X - 1) \quad (6)$$

allows F to be obtained directly, without explicitly determining the transmission configuration $\{\tau_{i,\sigma}\}$.

To obtain statistically meaningful results, ensembles of atomic contacts were analyzed across four different samples. For the purpose of probing spin filtering signatures in Cu_xO junctions [cf. Fig. 4 (b)], we are primarily interested in the conductance range below $1G_0$ [16, 17], which is the regime where the Fano factor analysis allows the detection of a potential SP [22]. Noise spectra were acquired for each configuration at discrete bias voltages and analyzed following the procedure that is outlined in [22] (see SI for detailed information).

For all junctions exhibiting a sufficiently constant dI/dV characteristics over the bias range of the noise measurements, we focus on their representation in the

$F(G)$ space. The analysis as depicted in Fig. 4 (c) shows that the majority of data points lies above the spin degenerate single-channel limit (black solid line), indicating that charge transport involves more than one spin degenerate channel. In this situation, the Fano factor does not allow conclusions about spin polarized currents since any enhancement of F , whether due to a multichannel situation or orbital degeneracy, would overcompensate the noise reduction induced by SP [22]. Our investigation shows, however, that a minute fraction of contacts falls indeed within the regime that is not compatible with transport through a single, spin degenerate channel. We present two examples in Fig. 4, where the noise spectra for each contact are shown in (d) and the corresponding noise-voltage $Y(X)$ are given in (e). In both cases, we observe a partial SP of about 60% and 45%, as illustrated by the two red star-filled data points in (c). Across all investigated samples, the extracted value varies between 40% and 100%, indicating that the degree of spin selectivity can differ substantially among different Cu_xO junctions.

2. Anomalous shot noise and Kondo resonance

As a next step, we go beyond the conventional Fano factor analysis, the interpretation of which is more involved by the presence of at least two contributing channels. The focus is set on contacts with strongly nonlinear I - V characteristics featuring a pronounced ZBA. Despite the fact that our measurement procedure does not allow for temperature or magnetic-field dependent studies, there are reasonable arguments to interpret spectroscopic features, as exemplarily shown in Fig. 5 (a), as an emerging Kondo resonance. On contacts of this type, the excess noise $S_{I,ex}(V) = S_I(V) - S_I(0)$ exhibits a nonlinear dependence on the bias voltage, which cannot be simply captured by Eq. (4).

In the classical Landauer picture, transport properties are typically treated within the linear-response regime, implying that G and S_I depend on constant transmission coefficients. If this assumption fails, it becomes necessary to incorporate nonlinearities into an extended model. To link both observations, we build on the work of Tewari *et al.* [35] and Mu *et al.* [36], who reported on the anomalous shot noise arising in atomic-scale junctions with non-trivial potential barriers. Allowing the transmission function $T(E)$ to be energy dependent provides a natural way to account for nonlinear bias scaling in both the current and its non-equilibrium fluctuations. Their specific functional behavior depends on $T(E) = \sum_{i,\sigma} \tau_{i,\sigma}(E)$, which in general may consist of several energy dependent spin channel contributions. In the zero-temperature limit, the shot noise can then be written as

$$S_I(V) = G_0 \sum_{i,\sigma} \int_{-eV/2}^{eV/2} \tau_{i,\sigma}(E) [1 - \tau_{i,\sigma}(E)] dE \quad (7)$$

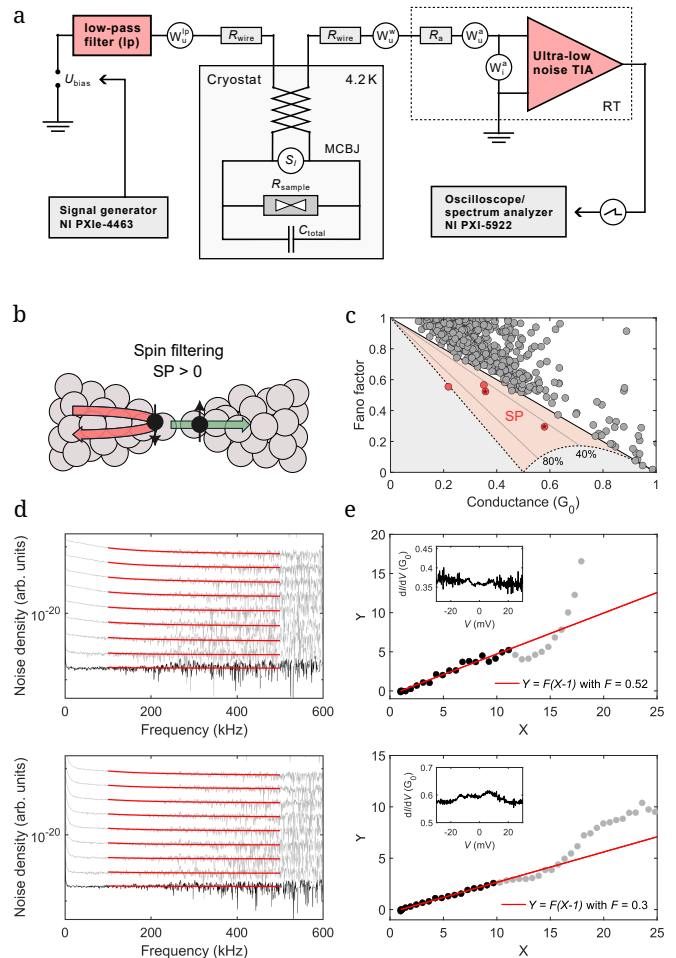


FIG. 4. (a) Circuit diagram of the electronic setup for measuring shot noise at low temperatures. (b) A Cartoon depicting the spin selectivity of an atomic Cu_xO junction. (c) Fano factor analysis in the $F(G)$ space, with the red data points highlighting contacts entering the spin polarized transport regime (red area). The noise spectra for two contact with SP along with fits to Eq. (D8) are shown in (d). Black spectra correspond to the zero-bias (thermal) noise, while gray spectra are obtained under non-equilibrium conditions with increasing bias from bottom to top and shifted vertically for clarity. The plots (e) display the noise-voltage characteristics in reduced units X and Y , together with a linear fit to the function $Y = F(X - 1)$ to extract the Fano factor F . The dI/dV curves are shown in the insets.

where the integration extends over the energy window eV set by the potential difference V . To determine the transmission function experimentally, we start from the measured $I - V$ characteristics and their numerical derivative. The differential conductance is fitted by the Fano formula given in Eq. (2), yielding an analytical function $(dI/dV)_{\text{fit}}(V)$, as exemplarily shown by the red line in Fig. 5 (a). After the successful parametrization and, hence, capturing the physics of the Kondo related ZBA,

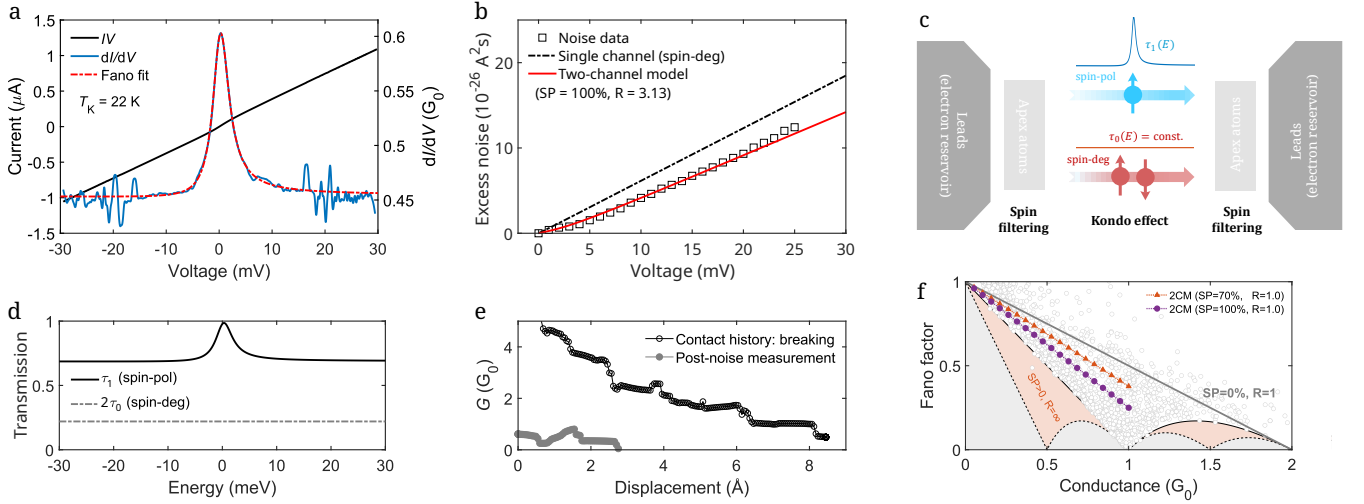


FIG. 5. Noise modeling on an atomic contact exhibiting a strong Kondo resonance: (a) IV and dI/dV characteristics, together with the Fano fit used to extract $T(E)$. (b) Excess noise $S_{I,ex}(V)$ compared with noise modeling that includes an energy dependent transmission. Calculations for the spin degenerate single-channel model (dash-dotted line) and the 2CM (red line) are shown. (c) Sketch of the 2CM applied to a Cu_xO atomic junction: A spin degenerate channel with a bias independent transmission τ_0 , together with a spin polarized channel, defines the transmission of the monoatomic constriction. The polarized channel exhibits an energy dependent transmission function $\tau_1(E)$ and carries the profile of the Kondo resonance, which is induced by the magnetic moments of the Cu-O units. Additional spin filtering may occur in the nanoscale vicinity of the apex atoms, where surface magnetism in oxidized Cu becomes more dominant. (d) Transmission functions underlying the 2CM in (b) with $SP = 100\%$ and $R = 3.13$ (e) Conductance versus displacement before and after the noise measurement. (f) $F(G)$ plot interpreted within the 2CM. Two exemplary lines with fixed values of R and SP are indicated by colored marker symbols.

the resulting total transmission

$$T(E) = \frac{1}{G_0} \left(\frac{dI}{dV} \right)_{\text{fit}} (V) \quad (8)$$

serves as the basis for the subsequent modeling of the noise characteristics. As shown in Fig. 5 (b), interpreting $T(E)$ as a single spin degenerate channel leads to calculated excess noise that exceed the measured data. Similarly, the conductance measurements suggest that more than one spin channel is active in order to reach conductances larger than $0.5 G_0$. To empirically account for all measured Cu_xO junctions showing anomalous shot noise in the presence of a strong zero-bias peak (see SI for more examples), we construct a minimal two-channel model (2CM), which is sketched in Fig. 5 (c). In this model, one channel $\tau_1(E)$ is spin polarized and carries the energy dependent profile of the Kondo resonance, while the second channel τ_0 is spin degenerate and energy independent, providing a constant background contribution. As discussed below in Sec. IV, the SP may arise from the apex atoms, interconnecting the macroscopic leads with the central constriction. Their full transmission is

$$T(E) = 2\tau_0 + \tau_{1,\uparrow}(E) + \tau_{1,\downarrow}(E) \quad (9)$$

and the zero-temperature shot noise is obtained by sum-

ming the spin resolved contributions of each channel:

$$S_{I,2CM}(V) = G_0 \sum_{\sigma=\uparrow,\downarrow} \int_{-eV/2}^{eV/2} \tau_{1,\sigma}(E) [1 - \tau_{1,\sigma}(E)] dE + 2eVG_0 \tau_0(1 - \tau_0). \quad (10)$$

For a more detailed derivation of Eq. (10) and the technical procedure behind concrete calculations, the reader is referred to the SI. We parametrize the 2CM by two parameters: (1) the SP of the Fano active channel with

$$SP = \frac{|\tau_{1,\uparrow} - \tau_{1,\downarrow}|}{\tau_{1,\uparrow} + \tau_{1,\downarrow}}, \quad (11)$$

and (2) the relative contribution of the two channels, captured by the transmission ratio

$$R = \frac{\tau_1(E \gg k_B T_K)}{2\tau_0}. \quad (12)$$

By adjusting SP and R , the model quantitatively reproduces the measured excess noise versus bias for all contacts, as explicitly shown by the red line in Fig. 5 (b). The corresponding transmission functions underlying the 2CM for $SP = 100\%$ and $R = 3.13$ are shown in Fig. 5 (d). Additional insight into the contact configuration is provided by the contact history in Fig. 5 (e), where the conductance, plotted as a function of electrode displacement, indicates the formation of a short atomic chain of approximately 2 \AA during the noise measurements. Upon further elongation, the junction can be

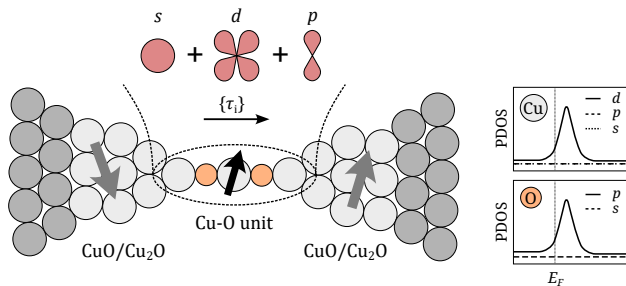


FIG. 6. Sketch of a Cu_xO atomic junction: The transmission properties are governed by a monoatomic chain of Cu-O units bridging the two electrodes. The interplay of all contributing orbitals gives rise to a net magnetic moment and spin polarized currents, predominantly hosted by the d and p orbitals of the Cu and O atoms, respectively. Surface oxidation at the outermost apex atoms may induce a finite magnetization that affects the transport properties. The projected density of states (PDOS) is cartooned following [17].

stretched by additional $\sim 2.5 \text{ \AA}$ before entering the tunneling regime. The total displacement, together with the non-monotonic conductance evolution during stretching, supports the conclusion that oxygen is involved in the contact formation.

Finally, after providing an additional argument for the involvement of two conduction channels, we revisit the Fano factor analysis and interpret it within the notation of the 2CM. For fixed combinations of SP and R and assuming $G = G_0 T(E)$, an array of $F(G)$ curves can be calculated. In the range $G < G_0$, these curves form straight lines, such as the one indicated by the colored marker symbols in Fig. 5 (f), which confirm the expected anticorrelation between F and SP . Most data points lie below the upper limit of maximum noise (gray line), where the conductance would be carried by two equivalent spin degenerate channels. These observations consistently underlines the two-channel picture in Cu_xO atomic junction.

IV. MINIMAL MODEL OF A Cu_xO ATOMIC JUNCTION

Our experimental findings suggest that the transport properties of oxidized Cu break junctions are governed by Cu-O entities forming the narrowest part of the constriction. While the macroscopic Cu electrodes can be treated as diamagnetic reservoirs, surface oxidation is expected to become more dominant closer to the constriction, where the conductor narrows down to the nanoscale. In a minimum model as schematically illustrated in Fig. 6, non-stoichiometric effects and surface magnetism may induce a finite magnetization in the vicinity of the apex atoms (light gray atoms). Such magnetic moments (gray arrows) are known to couple to the conduction electrons, with the capacity to act as spin polarizers or to generate non-monotonic MC signals.

Following theoretical predictions [16], we assume that Cu-O chains host ferromagnetic ground states, giving rise to a net magnetic moment (black arrow). For geometries with at least two incorporated oxygen atoms, this ground state also leads to spin polarized transmission channels. The dominant contributions arise from hybridized $\text{O}(2p)$ and $\text{Cu}(3d)$ orbitals, which form partially transmitting channels near the Fermi level [17].

Motivated by the Fano factor statistics and the Kondo analysis, a minimal transport description must include at least two effective channels. From an experimental perspective, the precise orbital composition of the transport channels – i.e., the relative contributions of s , p and d states – cannot be determined unambiguously. Nonetheless, all relevant orbitals should be regarded as potential contributors to transport.

V. CONCLUSION

In conclusion, we investigated the transport properties of air oxidized Cu MCBJs using a combination of magneto-transport, dI/dV spectroscopy, and shot noise measurements. The experiments consistently point toward the emergence of local magnetic moments in Cu_xO atomic contacts as predicted by theory [16, 17]. Specifically, the non-monotonic MC signals with large relative amplitudes indicate the presence of magnetic scattering centers in and around the constriction. The detection of ZBA with Fano line shapes complements this picture as it underscores the possible formation of Kondo resonances associated with the localized Cu_xO moments.

Shot noise spectroscopy provides complementary information on the underlying transport channels. While the Fano factor analysis of most contacts below one G_0 highlights their multichannel nature, it also reveals, through a small fraction of contacts compatible with a single channel, that (partially) spin polarized currents may occur. For junctions with strong ZBA, the excess noise shows an anomalous bias dependence that goes beyond the linear Landauer formalism. We introduce a minimal 2CM which acquires an energy dependent transmission function that carries the profile of the Kondo resonance and, hence, allows for a nonlinear noise modeling. Comparing the model based calculation with our experimental data, similarly suggests the presence of SP, which, remarkably, coexist with the Kondo correlations. We interpret this coexistence as another hint for the emergence of a local magnetization in the nanoscale vicinity of the apex atoms, likely induced by surface oxidation.

Taken together, these experimental findings provide a first coherent demonstration that oxygen incorporation into Cu nanocontacts can indeed induce localized magnetic moments and spin dependent transport at the atomic scale.

ACKNOWLEDGMENTS

We thank Theodoulos Costi and Oren Tal for helpful discussion and the staff of the nano.lab of the Univer-

sity of Konstanz for technical support. We gratefully acknowledge financial support from the DFG under project ID 493158779 as part of the collaborative research project SFB F 86 Q-M&S funded by the Austrian Science Fund (FWF) project number LAP 8610-N.

-
- [1] S. E. Bogenrieder, J. Beßner, A. K. Engstfeld, and T. Jacob, First-principles study on the structural and magnetic properties of low-index Cu_2O and CuO surfaces, *The Journal of Physical Chemistry C* **128**, 9693 (2024).
- [2] T. Kimura, Y. Sekio, H. Nakamura, T. Siegrist, and A. Ramirez, Cupric oxide as an induced-multiferroic with high- T_c , *Nature Materials* **7**, 291 (2008).
- [3] P. J. Brown, T. Chattopadhyay, J. B. Forsyth, and V. Nunez, Antiferromagnetism in CuO studied by neutron polarimetry, *Journal of Physics: Condensed Matter* **3**, 4281 (1991).
- [4] M. Ain, A. Menelle, B. M. Wanklyn, and E. F. Bertaut, Magnetic structure of CuO by neutron diffraction with polarization analysis, *Journal of Physics: Condensed Matter* **4**, 5327 (1992).
- [5] P.-H. Shih, J.-Y. Ji, Y.-R. Ma, and S. Y. Wu, Size effect of surface magnetic anisotropy in Cu_2O nanoparticles, *Journal of Applied Physics* **103**, 07B735 (2008).
- [6] E. Batsaikhan, C.-H. Lee, H. Hsu, C.-M. Wu, J.-C. Peng, M.-H. Ma, S. Deleg, and W.-H. Li, Largely enhanced ferromagnetism in bare CuO nanoparticles by a small size effect, *ACS Omega* **5**, 3849 (2020).
- [7] S. Rehman, A. Mumtaz, and S. Hasanain, Size effects on the magnetic and optical properties of CuO nanoparticles, *Journal of Nanoparticle Research* **13**, 2497 (2011).
- [8] D. Gao, G. Yang, J. Li, J. Zhang, J. Zhang, and D. Xue, Room-temperature ferromagnetism of flowerlike CuO nanostructures, *The Journal of Physical Chemistry C* **114**, 18347 (2010).
- [9] H. Qin, Z. Zhang, X. Liu, Y. Zhang, and J. Hu, Room-temperature ferromagnetism in CuO sol-gel powders and films, *Journal of Magnetism and Magnetic Materials* **322**, 1994 (2010).
- [10] D. Gao, J. Zhang, J. Zhu, J. Qi, Z. Zhang, W. Sui, H. Shi, and D. Xue, Vacancy-mediated magnetism in pure copper oxide nanoparticles, *Nanoscale research letters* **5**, 769 (2010).
- [11] R. Das, J. Alonso, E. Jefremovas, L. Fernández Barquín, P. Ngoc, H. Nguyen, D. Viet, P. Vinh, and A. Duong, Suppression of ferromagnetic order in $\text{CuO}/\text{Cu}_2\text{O}$ nanocomposites, *Materials Today Communications* **32**, 104038 (2022).
- [12] G. Prabhakaran and R. Murugan, Room temperature ferromagnetic properties of Cu_2O microcrystals, *Journal of Alloys and Compounds* **579**, 572 (2013).
- [13] A. Aiswarya Raj, G. Madhu, and V. Biju, Nanostructured CuO with antiferromagnetic core and weakly ferromagnetic shell, *Journal of Solid State Chemistry* **278**, 120911 (2019).
- [14] C. Chen, L. He, L. Lai, H. Zhang, J. Lu, L. Guo, and Y. Li, Magnetic properties of undoped Cu_2O fine powders with magnetic impurities and/or cation vacancies, *Journal of Physics: Condensed Matter* **21**, 145601 (2009).
- [15] A. Soon, X.-Y. Cui, B. Delley, S.-H. Wei, and C. Stampfl, Native defect-induced multifarious magnetism in non-stoichiometric cuprous oxide: First-principles study of bulk and surface properties of $\text{Cu}_{2-\delta}\text{O}$, *Phys. Rev. B* **79**, 035205 (2009).
- [16] D. Çakır and O. Gülseren, Effect of impurities on the mechanical and electronic properties of Au, Ag, and Cu monatomic chain nanowires, *Phys. Rev. B* **84**, 085450 (2011).
- [17] X. Zheng, Y.-Q. Xie, X. Ye, and S.-H. Ke, Conductance and spin-filter effects of oxygen-incorporated Au, Cu, and Fe single-atom chains, *Journal of Applied Physics* **117**, 043902 (2015).
- [18] W. H. A. Thijssen, M. Strange, J. M. J. van de Brugh, and J. M. van Ruitenbeek, Formation and properties of metal-oxygen atomic chains, *New Journal of Physics* **10**, 033005 (2008).
- [19] S. Chakrabarti, A. Vilan, G. Deutch, A. Oz, O. Hod, J. E. Peralta, and O. Tal, Magnetic control over the fundamental structure of atomic wires, *Nature communications* **13**, 4113 (2022).
- [20] J. M. van Ruitenbeek, A. Alvarez, I. Piñeyro, C. Grahmann, P. Joyez, M. H. Devoret, D. Esteve, and C. Urbina, Adjustable nanofabricated atomic size contacts, *Review of Scientific Instruments* **67**, 108 (1996).
- [21] F. Strigl, C. Espy, M. Bückle, E. Scheer, and T. Pietsch, Emerging magnetic order in platinum atomic contacts and chains, *Nature Comm.* **6**, 6172 (2015).
- [22] M. W. Prestel, M. Strohmeier, W. Belzig, and E. Scheer, Revealing channel polarization of atomic contacts of ferromagnets and strong paramagnets by shot-noise measurements, *Phys. Rev. B* **104**, 115434 (2021).
- [23] M. Strohmeier, K. Kirchberger, and E. Scheer, Nonlinear transport properties of atomic copper point contacts, *Low Temperature Physics* **49**, 827 (2023).
- [24] B. Ludoph and J. M. v. Ruitenbeek, Conductance fluctuations as a tool for investigating the quantum modes in atomic-size metallic contacts, *Phys. Rev. B* **61**, 2273 (2000).
- [25] R. Vardimon, M. Matt, P. Nielaba, J. C. Cuevas, and O. Tal, Orbital origin of the electrical conduction in ferromagnetic atomic-size contacts: Insights from shot noise measurements and theoretical simulations, *Phys. Rev. B* **93**, 085439 (2016).
- [26] F. Strigl, M. Keller, D. Weber, T. Pietsch, and E. Scheer, Magnetism in Pd: Magnetoconductance and transport spectroscopy of atomic contacts, *Phys. Rev. B* **94**, 144431 (2016).
- [27] M. W. Prestel, M. F. Ritter, A. Di Bernardo, T. Pietsch, and E. Scheer, Tuning the magnetic anisotropy energy of atomic wires, *Phys. Rev. B* **100**, 214439 (2019).
- [28] M. R. Calvo, J. Fernandez-Rossier, J. J. Palacios, D. Jacob, D. Natelson, and C. Untiedt, The Kondo effect in ferromagnetic atomic contacts, *Nature* **458**, 1150 (2009).
- [29] M. R. Calvo, D. Jacob, and C. Untiedt, Analysis of

- the kondo effect in ferromagnetic atomic-sized contacts, *Phys. Rev. B* **86**, 075447 (2012).
- [30] H. E. van den Brom and J. M. van Ruitenbeek, Quantum suppression of shot noise in atom-size metallic contacts, *Phys. Rev. Lett.* **82**, 1526 (1999).
- [31] R. Vardimon, M. Klionsky, and O. Tal, Experimental determination of conduction channels in atomic-scale conductors based on shot noise measurements, *Phys. Rev. B* **88**, 161404 (2013).
- [32] A. Burtzloff, A. Weismann, M. Brandbyge, and R. Berndt, Shot noise as a probe of spin-polarized transport through single atoms, *Phys. Rev. Lett.* **114**, 016602 (2015).
- [33] Y. Blanter and M. Büttiker, Shot noise in mesoscopic conductors, *Physics Reports* **336**, 1 (2000).
- [34] M. Kumar, R. Avriller, A. L. Yeyati, and J. M. van Ruitenbeek, Detection of vibration-mode scattering in electronic shot noise, *Phys. Rev. Lett.* **108**, 146602 (2012).
- [35] S. Tewari and J. van Ruitenbeek, Anomalous nonlinear shot noise at high voltage bias, *Nano Letters* **18**, 5217 (2018).
- [36] A. Mu, O. Shein-Lumbroso, O. Tal, and D. Segal, Origin of the anomalous electronic shot noise in atomic-scale junctions, *The Journal of Physical Chemistry C* **123**, 23853 (2019).

Appendix A: Two-channel noise modeling

The formal description of the anomalous shot noise follows the Landauer formalism and is partly motivated by the work of Tewari *et al.* [35] and Mu *et al.* [36]. The starting point is the energy dependent transmission function $T(E)$ extracted from the differential conductance using the Fano fit described in the main text. Within the 2CM this transmission is decomposed into a spin polarized channel $\tau_1(E)$ and a spin degenerate background channel τ_0 . The spin resolved transmission can therefore be written as

$$T(E) = \sum_{i,\sigma} \tau_{i,\sigma}(E) = \tau_{0,\uparrow} + \tau_{0,\downarrow} + \tau_{1,\uparrow}(E) + \tau_{1,\downarrow}(E) \quad (\text{A1})$$

$$= 2\tau_0 + \tau_1(E) \quad (\text{A2})$$

with $\tau_{0,\uparrow} = \tau_{0,\downarrow} = \tau_0$. The polarized channel is expressed through the spin polarization parameter SP ,

$$\tau_{1,\uparrow}(E) = \left(\frac{1+SP}{2} \right) \tau_1(E), \quad (\text{A3})$$

$$\tau_{1,\downarrow}(E) = \left(\frac{1-SP}{2} \right) \tau_1(E). \quad (\text{A4})$$

In the zero-temperature limit the current follows from the Landauer expression

$$I(V) = \frac{e}{h} \int_{-eV/2}^{eV/2} T(E) dE = \frac{e}{h} \int_{-eV/2}^{eV/2} [\tau_1(E) + 2\tau_0] dE. \quad (\text{A5})$$

The corresponding shot noise is obtained by summing the partition noise contributions of all spin channels,

$$S_{I,2\text{CM}}(V) = G_0 \sum_{i,\sigma} \int_{-eV/2}^{eV/2} \tau_{i,\sigma}(E) [1 - \tau_{i,\sigma}(E)] dE. \quad (\text{A6})$$

Substituting the spin resolved transmissions yields

$$\begin{aligned} S_{I,2\text{CM}}(V) &= G_0 \int_{-eV/2}^{eV/2} \left(\frac{1+SP}{2} \right) \tau_1(E) \left[1 - \left(\frac{1+SP}{2} \right) \tau_1(E) \right] dE \\ &+ G_0 \int_{-eV/2}^{eV/2} \left(\frac{1-SP}{2} \right) \tau_1(E) \left[1 - \left(\frac{1-SP}{2} \right) \tau_1(E) \right] dE \\ &+ 2eVG_0 \tau_0(1 - \tau_0). \end{aligned} \quad (\text{A7})$$

The parameters SP and R are defined in Eqs. (11) and (12). For a given parameter pair, τ_0 and $\tau_1(E)$ follow from the condition

$$T(E) = 2\tau_0 + \tau_1(E). \quad (\text{A8})$$

The calculated noise $S_{I,2\text{CM}}(V)$ is then compared with the experimentally measured excess noise. The transmission ratio R determines the relative contribution of the two channels at large bias

$$R = \frac{\tau_1(E \gg k_B T_K)}{2\tau_0}. \quad (\text{A9})$$

Two limiting regimes can therefore be distinguished

$$\begin{aligned} R < 1 &: \quad \text{if } \tau_0 \text{ dominates } G(|V| \gg k_B T_K) \\ R > 1 &: \quad \text{if } \tau_1 \text{ dominates } G(|V| \gg k_B T_K) \end{aligned}$$

These limits provide a convenient way to interpret the transport characteristics of the junction within the suggested two-channel description for atomic-scale Cu_xO junctions.

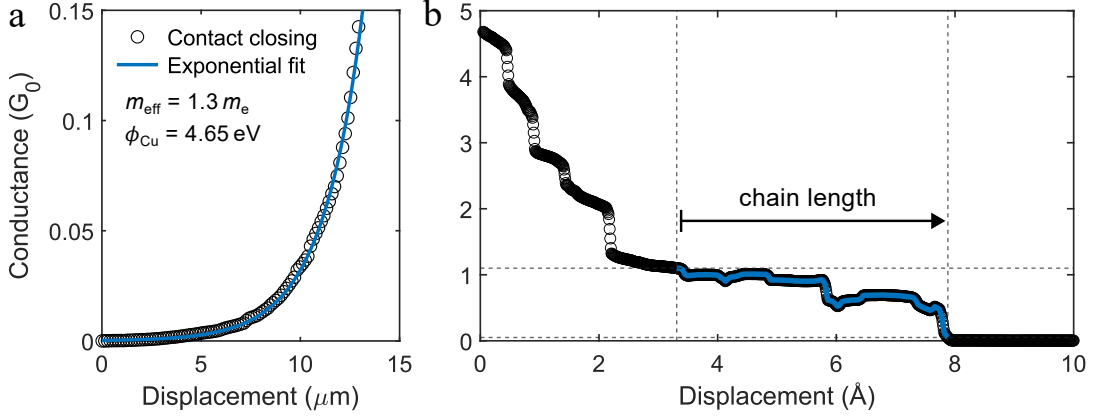


FIG. 7. (a) Exponential increase of the tunnel conductance when closing the break junction, leading to the formation of an atomic-size contact. Fitting the trace with respect to the displacement (solid line) can be used to calculate the reduction ratio r , necessary for the calibration of the horizontal displacement of the junction. (b) Example of an opening trace illustrating the definition of the chain length used in the analysis: as indicated by the dashed lines, the length is defined as the displacement between the two points where the conductance drops below 1.1 and $0.05 G_0$, respectively. After calibration, the conductance trace attributed to the atomic-size chain (bluish solid line) typically evolves over elongations on the order of a few angstroms.

Appendix B: Calibration of the electrode displacement

The determination of atomic chain lengths requires a calibration of the mechanical displacement in the break junction experiment. The bending mechanics produces a vertical substrate displacement Δz , which translates into a horizontal elongation of the junction Δu . The relation between both quantities is described by the reduction ratio $r = \Delta u / \Delta z$ [20].

The calibration of r uses the exponential dependence of the tunneling conductance on the electrode separation. When the junction approaches the closure, the conductance follows an exponential functional evolution

$$G \sim \exp\left(\frac{2}{\hbar} \sqrt{2m_{\text{eff}}\phi} \cdot \Delta u\right), \quad (\text{B1})$$

where m_{eff} denotes the effective electron mass and ϕ the work function of the material. Expressing the elongation through $\Delta u = r \Delta z$ yields the fit function

$$G(\Delta z) = A \exp\left(\frac{2}{\hbar} \sqrt{2m_{\text{eff}}\phi} r \Delta z\right), \quad (\text{B2})$$

with Δz given in units of μm . A representative fit to an experimental trace is shown in Fig. 7 (a). Due to the absence of reliable parameters for the Cu_xO junction, both m_{eff} and ϕ are approximated by the values reported for Cu (see inset). Closing traces may show deviations from a purely exponential behavior close to $1 G_0$, which likely originate from structural rearrangements in Cu_xO configurations. These deviations are not included in the fit. Instead, the reduction ratio r is exclusively verified on pristine traces recorded on a particular sample.

After calibration, the horizontal electrode displacement can be expressed in absolute units. Fig. 7 (b) shows an example of a calibrated opening trace. The elongation of an atomic contact typically occurs over a displacement of a few angstroms. The chain length is defined following the procedure introduced by Thijssen *et al.* [18]. For each opening trace, the two positions at which the conductance drops below $1.1 G_0$ and $0.05 G_0$, respectively, are determined. The displacement between these points defines the chain length. Within this interval (indicated by the black arrow) the conductance often exhibits a non-monotonic evolution that consists of several discrete jumps. These features reflect structural rearrangements during the final stage of the chain elongation.

Appendix C: Additional examples of Kondo active junctions

In Figs. 8 and 9 we present further noise and transport measurements on atomic-scale Cu_xO junctions exhibiting a pronounced Kondo resonances. In all cases, the (anomalous) excess noise is similarly compared with the noise modeling (2CM) as described in the main text.

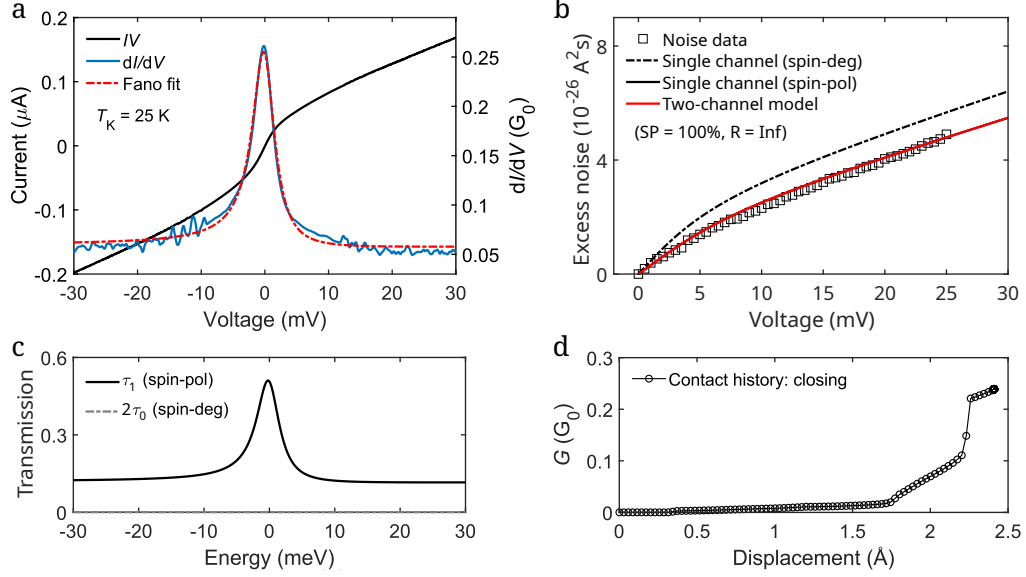


FIG. 8. Noise modeling on contact 2 exhibiting a strong Kondo resonance: (a) IV and dI/dV characteristics, together with the Fano fit used to extract $\tau(E)$. (b) Excess noise $S_{I,\text{ex}}(V)$ compared with noise modeling that includes an energy dependent transmission. Calculations for the spin degenerate single-channel model (dash-dotted line) and the 2CM (red line) are shown. (c) Transmission functions underlying the 2CM. (d) Conductance versus displacement before and after the noise measurement.

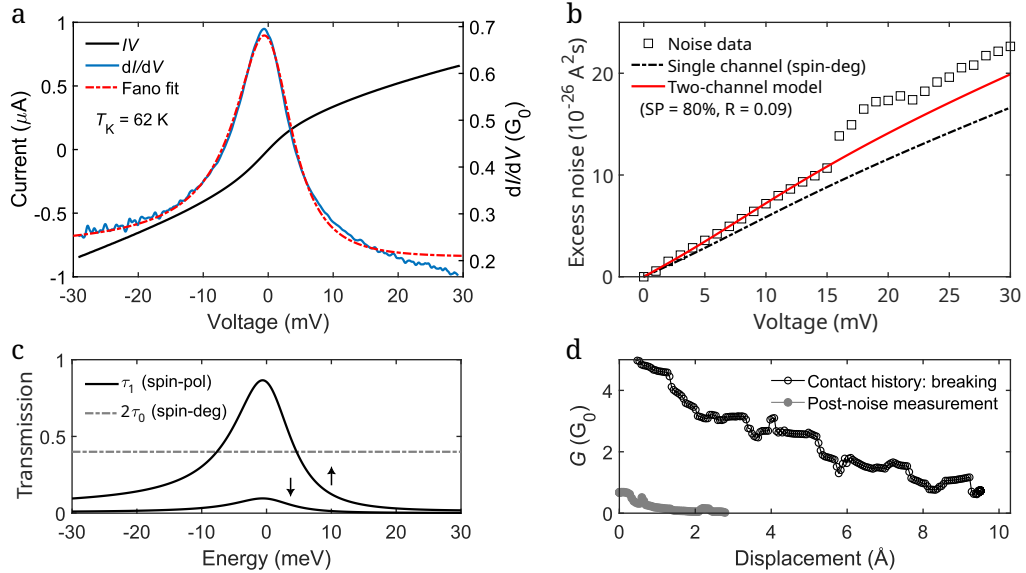


FIG. 9. Noise modeling on contact 3 exhibiting a strong Kondo resonance: (a) IV and dI/dV characteristics, together with the Fano fit used to extract $\tau(E)$. (b) Excess noise $S_{I,\text{ex}}(V)$ compared with noise modeling that includes an energy dependent transmission. Calculations for the single-channel models (dash-dotted and black solid line) and the 2CM (red line) are shown. (c) Transmission functions underlying the 2CM. (d) Conductance versus displacement before and after the noise measurement.

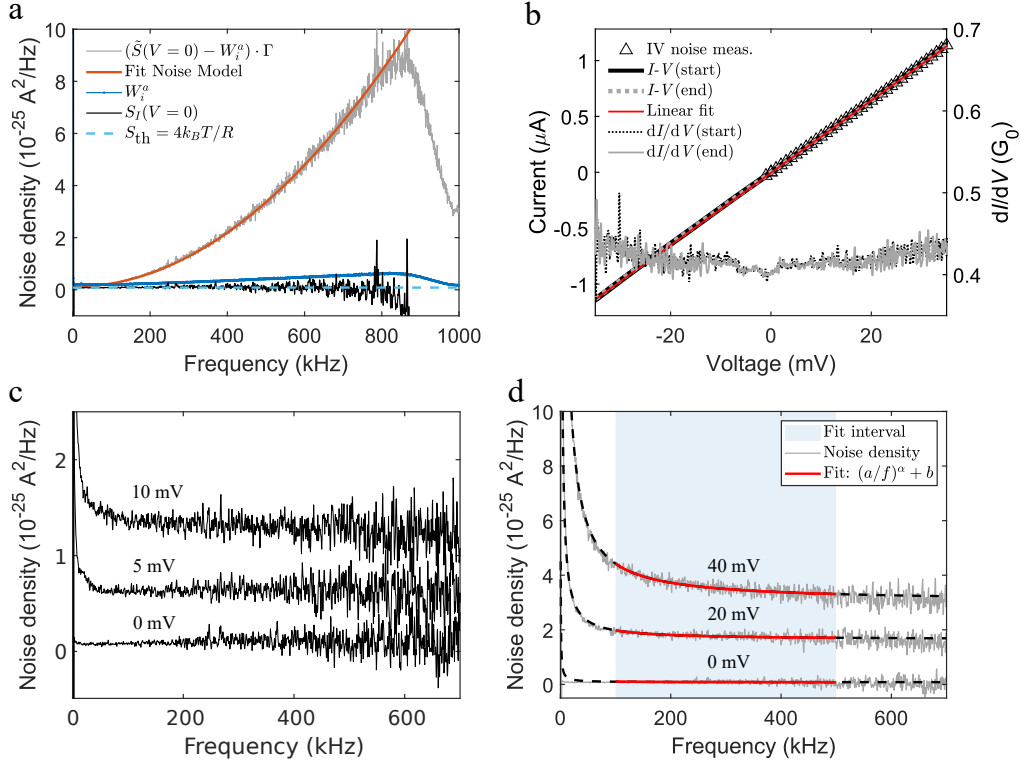


FIG. 10. Noise modeling and data postprocessing for one particular atomic contact: (a) Measured noise ($\tilde{S}(V=0) - W_i^a$) Γ (gray) and fit to the noise model of Eq. (D6) (red) using T and C_{total} as free parameters. A correction according to Eq. (D6) yields $S_I(V=0)$ (black), the sample's intrinsic current noise. At zero bias, S_I is equal to the thermal noise S_{th} (light-blue dashed), which falls in the same range as W_i^a (blue). (b) I - V characteristics and numerically computed dI/dV s measured prior and subsequent to the noise measurement to determine R_{sample} . (c) Corrected spectra $S_I(V)$ at varying bias voltage. (d) Fitting of the spectra $S_I(f)$ with the function $(a/f)^\alpha + b$ to account for $1/f^\alpha$ -type noise contributions, while extracting the white noise part $S_w := b$. The area shaded in blue indicates the fit interval.

Appendix D: Noise setup and modeling

Accurate shot noise measurements on atomic-scale contacts require a detailed modeling of the measurement circuit. The recorded signal contains contributions from several instrumental noise sources in addition to the intrinsic current fluctuations of the sample. A reliable extraction of the sample noise therefore requires a quantitative description of the full measurement setup, including its impedance and frequency response. In the following, the dominant noise sources of the setup are summarized and incorporated into an equivalent circuit model.

Four principal noise sources contribute to the measured signal.

(i) Low-pass filter (adder): The home-built adder stage operates as a low-pass filter and is placed behind the voltage source (NI PXIe-4463). Both the adder itself and the voltage source contribute voltage noise contributions.

(ii) Transimpedance amplifier (TIA): The TIA converts current fluctuations into a measurable voltage signal and introduces both current and voltage noise. The frequency dependent current noise W_i^a can be obtained directly from a noise spectrum recorded with an open input.

(iii) Wiring: The entire cabling between the room temperature electronics and the cryogenic insert produces a thermal voltage noise.

(iv) Sample (MCBJ): The mechanically controllable break junction generates the intrinsic current noise S_I of interest, which consists of thermal noise and bias dependent excess noise (shot noise).

Each noise contribution W is represented as an independent voltage or current source in an equivalent circuit shown in Fig. 4 (a). Capacitances originating from the sample, wiring, and electronic components are combined into an effective capacitance on the order of $C_{\text{total}} \sim 100$ pF. The sample resistance R_{sample} acts in parallel with this capacitance, forming a frequency dependent impedance that can be written as

$$\frac{1}{Z'} = i\omega C_{\text{total}} + \frac{1}{R_{\text{sample}}}. \quad (\text{D1})$$

This impedance appears in series with the remaining setup resistance $R_{\text{setup}} = R_{\text{wire}} + R_{\text{amp}}$, where R_{wire} accounts for the resistance of the cabling and R_{amp} represents the input resistance of the amplifier stage. The total impedance of the detection circuit therefore becomes

$$Z_{\text{total}} = Z' + R_{\text{setup}}. \quad (\text{D2})$$

With this, voltage noise contributions originating from the electronic components (and listed above) are converted into a measurable current noise by the impedance of the circuit. Their corresponding contribution to the measured noise spectrum is given by

$$\tilde{W}_i^{\text{setup}} = \frac{W_u^{\text{lp}} + W_u^{\text{a}} + W_u^{\text{w}}}{|Z_{\text{total}}|^2}. \quad (\text{D3})$$

At the same time, the intrinsic current noise S_I generated by the sample is filtered by the same circuit elements. As a result, the measured sample noise \tilde{S}_I is related to S_I via the relation

$$\tilde{S}_I = S_I \left| \frac{Z'}{Z_{\text{total}}} \right|^2, \quad (\text{D4})$$

which defines the transfer function of the measurement circuit

$$\mathcal{H} = \frac{\tilde{S}_I}{S_I} = \left| \frac{Z'}{Z_{\text{total}}} \right|^2. \quad (\text{D5})$$

Taking all instrumental noise sources of the whole circuit into account yields the complete model based analytical expression for the measured noise spectrum

$$\tilde{S} = S_I \left| \frac{Z'}{Z_{\text{total}}} \right|^2 + \frac{W_u^{\text{lp}} + W_u^{\text{a}} + W_u^{\text{w}}}{|Z_{\text{total}}|^2} + W_i^{\text{a}}. \quad (\text{D6})$$

To extract the intrinsic sample noise, the spectrum measured at zero bias $\tilde{S}(V=0)$ is used to initialize the model. At zero bias, the sample contribution reduces to the thermal noise $S_{\text{th}} = 4k_B T / R_{\text{sample}}$. Eq. (D6) can therefore be fitted using the temperature T and the total capacitance C_{total} as free parameters. A fit to a representative spectrum $\tilde{S}(V=0)$, along with the corrected spectra $S_I(V=0)$, W_i and the corresponding thermal noise S_{th} is illustrated in Fig. 10 (a). To obtain R_{sample} , IV curves are measured before and after each noise measurement [see Fig. 10 (b)]. With the calibrated capacitance C_{total} , spectra recorded at finite bias can be corrected according to the relation

$$S_I(f, V) = \left[(\tilde{S}(f, V) - W_i^{\text{a}}(f)) \Gamma(f) - \frac{W_u^{\text{lp}} + W_u^{\text{a}}(f) + W_u^{\text{w}}}{|Z_{\text{total}}|^2} \right] \left| \frac{Z'}{Z_{\text{total}}} \right|^{-2}, \quad (\text{D7})$$

as depicted in Fig. 10 (c). Note that within the Landauer-Büttiker framework thermal noise and shot noise should exhibit a white spectral density. Atomic contacts, however, may display additional frequency dependent contributions. Enhanced $1/f^\alpha$ noise in atomic junctions has been reported, particularly at elevated bias voltages [36]. To separate white noise from the frequency dependent component, each corrected spectrum is fitted with

$$S_I(f) = \left(\frac{a}{f} \right)^\alpha + b, \quad (\text{D8})$$

where a , b , and α are free parameters [see Fig. 10 (d)]. The constant term b defines the white-noise contribution $S_w := b$, which is used for the subsequent shot noise analysis. The fitting interval typically spans $f \in [100, 500]$ kHz, where the measurement bandwidth remains free from instrumental cutoff effects.